Atomic Force Microscopy and Raman Spectroscopy Study of Tantala Films

Dominic Hutley Lawson

Submitted as a thesis for the degree of MSc(R)

May 2014

Acknowledgements

After almost 3 years of working with the Materials and Condensed Matter Physics Group I would like to say a big thank you to my colleagues for the good times and what I have learnt from you all.

In particular I would like to say thank you to Dr Donald MacLaren for being my principle supervisor and for also spending a lot of time and effort to help me produce this document. I would like to thank him for the many valuable lessons I have learnt from him.

I have worked very closely with Professor Andrew Long, Dr Iain Martin and Andrew Monaghan on this piece of research. It has been a highly enjoyable experience as well as a privilege to be part of that team.

Abstract

This thesis contains a report of two distinct areas of research into thin films of tantalum pentoxide (Ta_2O_5), also known as tantala. Firstly, the surfaces of the tantala films have been investigated with atomic force microscopy (AFM) and the results presented and analysed. Secondly, the same films have been investigated with Raman spectroscopy and conclusions have been drawn from the data. Thin films of tantala are used as mirror coatings in gravitational wave detectors. Theoretically predicted gravitational waves should induce a movement of 10^{-20} m $Hz^{-1/2}$ in a gravitational wave detector. All sources of noise that could preclude the positive detection of a wave need to be minimised if not removed altogether. A mechanical dissipation within the tantala films is one such source of noise that limits the sensitivity of the detector. This mechanism is not altogether understood yet. In this work thin films of tantala (10-500nm) have been deposited by pulsed laser deposition (PLD), atomic layer deposition (ALD) and ion beam sputtering (IBS) on to silicon substrates. Studies by atomic force microscopy (AFM) have been made and show the influence of deposition conditions on the surface morphology of grown films. Films with low surface roughness will be good candidates for mirror coatings in order to minimise possible scattering of incident radiation. The same films have also been studied with Raman spectroscopy in an effort to characterise the vibrational energy of the films. Raman studies of glasses are relatively rare and this is a first study in the context of mirror coatings and doped tantala. An assessment is offered as to what films offer the best features for mirror coatings.

Contents

1. Introduction

1.1. Aims

The aim of this work is to present what tantala films are best suited to be used as mirror coatings in gravitational wave detectors. Tantala films that are smooth and without imperfections will reflect radiation. The AFM data are characterised in terms of surface roughness and therefore a low roughness is key to minimising scattering of incident radiation for the best mirror coating.

Raman spectroscopy is used to characterise the vibrational modes and thereby the nanoscale structure of the tantala films. Noise from mechanical dissipation within the tantala films will obscure the hoped-for detection of postulated gravitational waves. The vibrational modes of each film recorded with Raman spectroscopy might give an insight into a possible link between the vibrational modes and the mechanical dissipation. The associated experimental fabrication parameters of the films may then be linked to this mechanical dissipation also. It may then be possible to link the AFM and Raman studies to say which film is the best overall candidate for a mirror coating.

In this report I will discuss tantala and its use in gravitational wave detectors. I will then proceed to discuss the fabrication techniques used for the tantala films I have studied. I will then discuss how we then characterise the films with AFM and Raman spectroscopy. All results are then discussed and an overall conclusion is given.

1.2. Background of Tantalum Pentoxide (Ta_2O_5)

Tantalum pentoxide (Ta_2O_5) has a wide range of industrial applications. At least since the 1990s and up to the present day, Ta_2O_5 has received a huge amount of interest as a capacitor material due to its high dielectric constant of $\varepsilon = 25$ [1]. This dielectric constant is much higher than that of either SiO_2 or Si_3N_4/SiO_2, both of which have conventionally been used as insulators in the microelectronics industry [2] [3]. In particular, research has publicised the application of Ta_2O_5 in high density dynamic random access memory (DRAM) devices and for the use as gate dielectrics in metal - oxide - semiconductor (MOS) devices [4] [5]. Ta_2O_5 also has a high refractive index of $n = 2.2$ at 633 nm and a very large band gap of $Eg = 4.2\ eV$. Thus, it is almost absorption-free for wave-lengths ranging from 300 nm up to 2.0 mm [1], [6] - [10]. It is of great interest for optoelectronic applications such as light waveguides, as an anti-reflection coating for solar cells or charge coupled devices [1] [11], as a birefringent coating and as a component of multilayer interference filters [3] [6]. Another attractive application of Ta_2O_5 is the use as mirror coatings [12] e.g. in gravitational wave detection.

The properties of Ta_2O_5 films have been demonstrated to be strongly dependent on the deposition method, the nature of the film substrate and the post deposition annealing treatment. For the fabrication of thin films of Ta_2O_5 there are many deposition techniques currently in use. Low pressure metal organic chemical vapour deposition (LPMOCVD), plasma-enhanced CVD, UV photochemical CVD, magnetron sputtering, ion beam sputtering (IBS), metal organic solution deposition (MOSD), sol-gel deposition, atomic layer deposition (ALD) as well as pulsed laser deposition (PLD) [5] have all been used. In this current study IBS, ALD and PLD tantala films have been studied.

In the following section I will outline how tantala is used in the hunt for gravitational waves.

1.3. Ta_2O_5 for mirror coatings

Optical coatings for mirrors in gravitational wave detectors are typically multilayers of Ta_2O_5 and SiO_2. These mirrors reflect laser beams in a Michelson Interferometer. Gravitational waves are predicted to shift the length of these beams by less than 10^{-20} m $Hz^{-1/2}$ [13]. In order to observe such a minute displacement, all sources of noise must be reduced to the lowest level possible. Thermal noise arising from a mechanical dissipation is one such limiting factor in gravitational wave detection and it exists in Ta_2O_5 films [14].

In this thesis we had access to single films of Ta_2O_5 grown by IBS and ALD on silicon cantilevers. Silicon cantilevers are used as a substrate for the Ta_2O_5 films so as to establish the mechanical dissipation in them by a “ring down” experiment described in reference [14]. The cantilever with the thin film attached is forced to oscillate by the use of an electrostatic actuator, exciting a resonant mode. The oscillation is then allowed to decay freely in a vacuum at cryogenic temperatures in order to assess the degree and nature of mechanical dissipation. The oscillations are recorded by a laser beam incident on the cantilever system.

Along with the supplied IBS and ALD films, I personally deposited Ta_2O_5 films by PLD and therefore make a comparison of film quality between the different deposition methods. All films have been tested by AFM and Raman spectroscopy.

It has been reported that the mechanical dissipation in the Ta_2O_5 can be reduced by ~40% by doping the tantala with TiO_2 [15]. The coatings in the multilayer system are also usually heat treated to reduce the stress between the films and also to reduce optical absorption of incident radiation [16]. In [17] thermal treatment reduced the mechanical dissipation in bulk fused silica and so it is in [14] that the thermal treatment effect on Ta_2O_5 is presented. Heat treatment temperatures in the range of 100-800°C were used with lower heat treatment temperatures seeming to more effectively reduce the mechanical dissipation.

2. Theory of growth techniques

In this chapter I will present a theoretical description of pulsed laser deposition, ion beam sputtering and atomic layer deposition. I will also review the literature on the PLD of Ta_2O_5 and give details of the IBS and ALD films.

2.1. Pulsed Laser Deposition

The deposition technique I used to manufacture films of tantala was pulsed laser deposition (PLD). PLD was pioneered by Smith and Turner in 1965 [18] and became an established technique as of 1987 with the work Dijkkamp et al. [19]. PLD is a vapour deposition technique that uses laser ablation of a target. The quality of a deposited thin film is dependent on the properties of the laser and the optical, topological and thermodynamic properties of the target [20]. When a pulse from the laser (lasting 20ns) is absorbed at the target the electromagnetic energy is converted into electronic excitation and then to thermal, chemical and even mechanical energy that cause evaporation, ablation, excitation, plasma formation and exfoliation. This interaction causes material to be ejected from the target surface that expands towards a substrate ready to be coated. The ejected material forms a characteristic plume that is composed of a plasma of electrons, ions and energetic atoms and molecules in addition to up to micron sized solid masses known as clusters. The dense plume of material is directed towards the substrate in the vacuum chamber where it adheres as a film [20].

A schematic of a typical PLD system is shown in Figure 1. The system consists of a vacuum chamber equipped with pumps, pressure gauges and other instruments to control the deposition environment. Film growth can be carried out in a reactive gas atmosphere (such as O_2 for the deposition of oxides) or vacuum and with the ability to heat a substrate, a range of conditions can be accessed. With this versatility the phase diagram of a material can be probed. One can grow a film that is either amorphous or crystalline in addition to it being either epitaxial or not.

A PLD system may also have the capability for in situ monitoring of the growth process of a film with a Reflective High Energy Electron Diffraction (RHEED) system within the vacuum chamber (not illustrated in Figure 1). This provides a real time check of the crystalline quality of the film during deposition [20]. The specific pattern of diffraction spots would indicate the degree of crystallinity and also what type of growth mode type had taken place. By recording the intensity of the diffraction pattern during deposition a plot against time can be highly informative. An ideal growth case would reveal a sinusoidal wave where each new peak corresponds to the completion of another monolayer during deposition.

In order to prevent non-uniform target erosion, the target is typically rotated and/or rastered from side to side to make sure every possible location undergoes uniform laser

ablation. Perhaps one of the biggest problems with PLD is the occurrence of particulates in the deposited film seen as lumps of material on the film surface. These are the result of the explosion of particles (known as “splashing”) or fragmented lumps (exfoliation) due to thermal shock from the target [20].

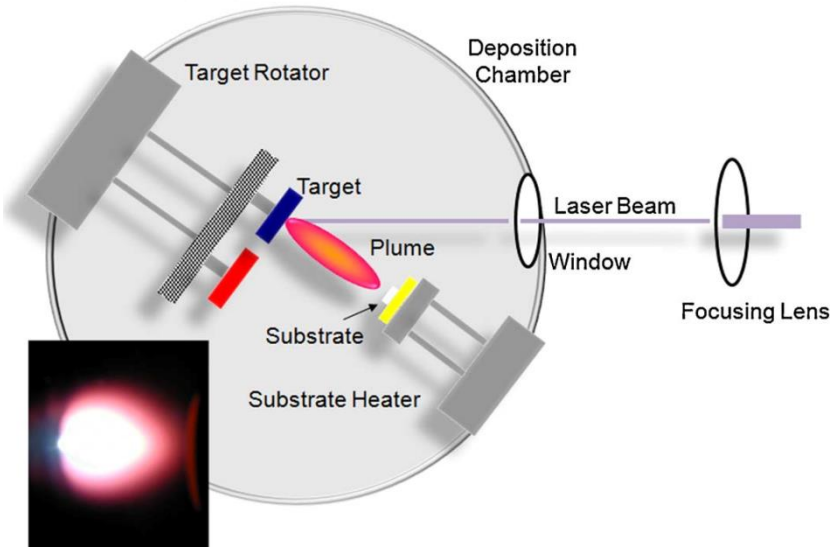

Figure 1 – The main components of a PLD system with a photograph of a plume of plasma generated during an ablation process. Both images are taken from reference [20].

2.2. PLD of Ta_2O_5

A number of studies have already examined the PLD of tantala films, leading to a set of experimental parameters for optimal deposition. Ta_2O_5 has been deposited extensively by PLD onto silicon, glass and quartz substrates. It is generally shown to be deposited as an amorphous film up to ~800°C, above which temperature it undergoes crystallisation. A post deposition anneal of ~800°C or greater will also promote crystalline β-Ta_2O_5 to form [1] [4] [5] [11]. X-ray diffraction (XRD) from reference [12] is shown in Figure 2 of Ta_2O_5 before (labelled (a)) and after (labelled (b)) annealing at 800°C for 30 minutes. A transition from amorphous to crystalline Ta_2O_5 is observed with the emergence of distinct diffraction peaks in Figure 2 (b).

Crystalline tantala films do not have the same reflection qualities or reported mechanical loss mechanism as amorphous films, so we must avoid crystallisation. It will be shown in chapter 4 that the surface of Figure 15 appears to be much rougher than all of the other films. It may well be the case that this film is making or has already made the transition from amorphous to crystalline tantala and therefore as a consequence the surface is now much rougher in appearance.

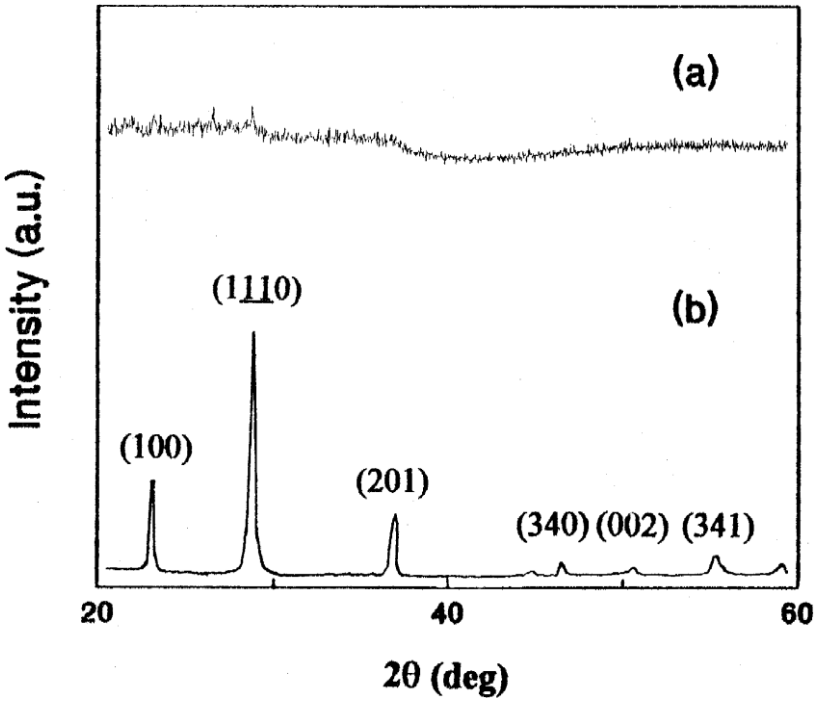

Figure 2 – X-ray diffraction spectra of Ta_2O_5 from reference [12] of (a) Ta_2O_5 deposited at 200°C and (b) after annealing the same film at 800°C [12].

From the studied literature, tantala films with the chemical composition of Ta_2O_5 are sought after for mirror coatings in gravitational wave detectors. The supplied IBS and ALD films are known to have either exactly the chemical composition of Ta_2O_5 or close to this stoichiometry. Therefore the PLD tantala films must match their IBS and ALD counterparts in terms of stoichiometry in order for a true comparison to take place. In order to proceed with depositing this material correctly an investigation into the oxygen gas pressure required for deposition was conducted. In most studies Rutherford Back Scattering (RBS) and Auger Electron Spectroscopy (AES) were used to test the stoichiometry of grown films. Table 1 is a summary of conditions that give the correct chemical composition. It can be seen from Table 1 that the O_2 gas pressure used is between 1 and 150mTorr for films with the correct stoichiometry. Anything out with this range can from the outset be ignored in deposition work. Also gas pressures lower than 11mTorr were not used when the deposition temperature exceeded 25°C. It would appear from the data that with increasing deposition temperature higher gas pressures are then used. This higher gas pressure may well be implemented to maintain the correct stoichiometry with the increased thermal energy effects at higher temperatures.

In reference [7] it was strongly asserted that a threshold of 37mTorr O_2 was the lowest pressure required that would ensure a Ta/O ratio of 0.4. After consulting the literature it was decided that 40mTorr O_2 would be used in all of my depositions.

Substrate Temperature (°C)	O_2 Pressure (mTorr)	Ta/O Ratio	Reference
25 150, 250,400 >800	1 ≥20 1	0.47±0.7 0.38±0.44 0.38±0.44	[1]
200	75	0.42	[5]
≥150	>20	0.38-0.44	[6]
25-400	11-150	0.4	[7]
200	75	0.42	[12]
25	37	≈0.4	[21]
600	150	0.42	[22]

Table 1 – Summary of the conditions for depositing tantala by PLD from studied literature.

As will be revealed in the results section of this report pits have been observed in PLD films. Pits have also been reported in some of the literature of the PLD of tantala. In reference [3] Ta_2O_5 depositions were carried out between 50-400°C and 10-100mTorr O_2. From Scanning Electron Microscopy (SEM), pits with a width <300nm but with no mention of the depth were observed in some cases. No reason was offered for their existence however. In the present application, size and frequency of pits and other imperfections must be kept to a minimum so as not to interfere detrimentally with beam reflections.

In reference [23] mixtures of O_2/He and also just O_2 were used in depositions. The mixture of oxygen and helium can allow for the correct oxygen level to be achieved but with the addition of further helium will constrain the plasma plume size. This will reduce both the lateral and vertical distance species in the plasma plume travel. Pits were observed for films deposited in O_2. With an O_2/He pressure of 13 and 94mTorr no pits were observed. SEM determined these films had the smoothest surfaces. There was a remarkable change for films deposited between 162 and 244mTorr. The films were much rougher and pits appeared in greater number for 244mTorr. The largest pits observed were 120nm in diameter. Also it was noted that for an O_2/He gas mix of 244mTorr deposits with a large size appear to constitute the film. An explanation was offered for the increased roughness. At higher O_2/He pressure, species have a longer residence time in the plasma plume. This is known as collisional relaxation [2] [3] [23]. It causes nucleation and growth of film forming precursor species in the plasma plume before reaching the substrate. This means a film will have deposits of large sizes and have an overall higher surface roughness. The longer the residence time of species in the plume, the larger the degree of nucleation and growth of vapour species. The result is a tantalum oxide film with larger deposits at 244mTorr O_2/He embedded in the surface. The conclusion is that collisional relaxation for Ta_2O_5 determines the surface roughness and microstructure of grown films. Therefore a moderate collisional relaxation of ejected species is better for the deposition of smooth and pit free films [21].

There wasn't an explicit reason given for the formation of pits but merely that in a lower He/O_2 gas mix films were less rough and didn't contain pits.

Particulates are reported to have been seen in films in references [1] [3] [5] [6] [12]. Particulates if big enough will be problematic for beam reflections and also in the case of the multilayer formation of Ta_2O_5 and TiO_2 layers. Particulates could make interfaces between layers irregular and make the films less uniform. SEM data show particulates with a diameter <1µm. These are thought to be molten globules ablated from the target surface.

2.3. Ion Beam Sputtering

A second technique used to deposit the films studied in this work was Ion beam sputtering (IBS). This deposition was method pioneered by Wei and Louderback in 1976 [24] and is widely used for the formation of high quality metal, alloy or oxide thin films [25].

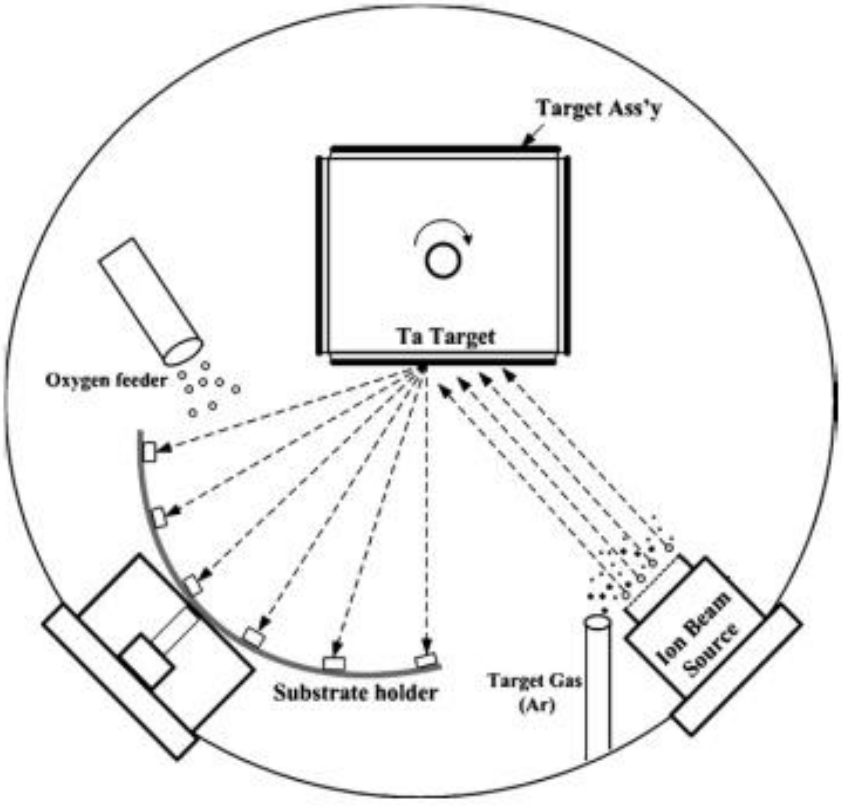

Figure 3 – IBS of Ta_2O_5 film in a vacuum chamber. Image taken from reference [26].

Figure 3 shows a typical IBS system. A tantalum (Ta) target is "sputtered" by inert gas ions e.g. Ar^+ ions from an ion gun in a vacuum chamber [24]. The sputtered Ta particles are then directed towards and ultimately deposited on to a substrate or substrates to form a film of Ta_2O_5 after having reacted with the background pressure O_2 molecules. High purity films with a low amount of defects are usually achieved as the kinetic energy of accelerated ions is effectively converted to a high mobility of species at the surface [27]. The separation

between the ion gun and the target is kept to a minimum to avoid possible contamination from material sputtered from outside the target. The sputtering efficiency is optimised with an ion beam angle of incidence on the target of greater than 50° [24]. Although ion bombardment can be accomplished in a number of ways the use of an ion beam is advantageous as great control is possible. The experimental parameters of ion current density, ion energy, the beam angle of incidence and ion species are accurately and independently controllable allowing for the fine tuning of film quality [28].

2.4. Atomic Layer Deposition

A third technique used to deposit films studied in this work was atomic layer deposition (ALD). This is a low temperature deposition method dominantly influenced by the surface chemistry and over layer formation mechanism [29]. During ALD solid layers that comprise a complete film grows via successive surface reaction cycles carried by inert gas flux into the reactor chamber [30].

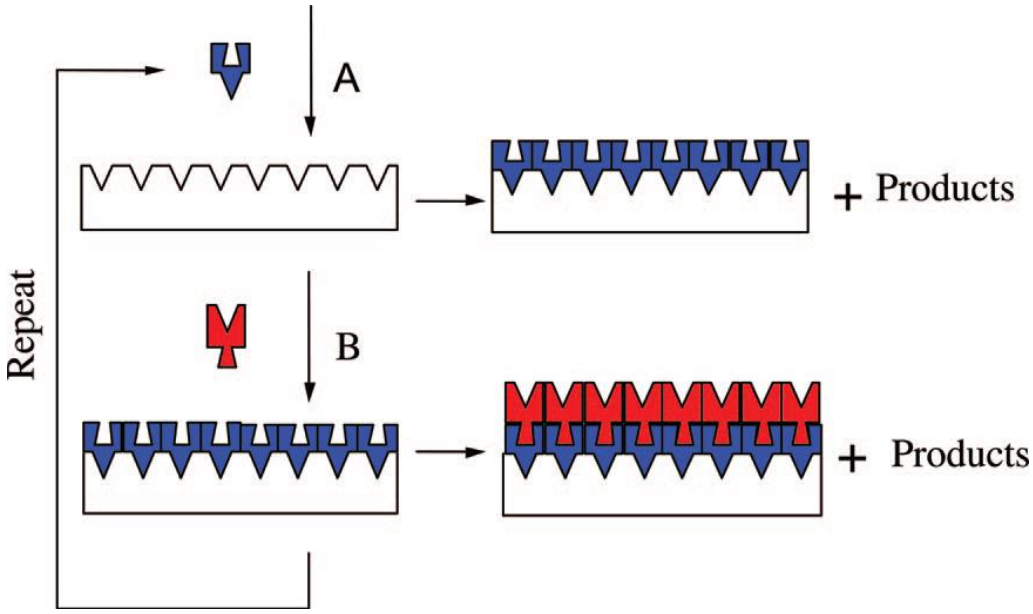

Figure 4 – A simplified atomic layer deposition process whereby a film is put down layer by layer in stages that are repeated until the desired film thickness is achieved [30].

Figure 4 shows a simple binary reaction sequence of a step A followed by a step B both known as precursor pulses. Step A can be taken as the deposition of a metal sub monolayer onto a substrate and step B is the subsequent deposition of the oxygen to form a single metal oxide layer. The process is self limiting as the capability of a surface to receive material is finite due to the finite nature of chemically active sites. After step A and step B there is a purge period. During the purge periods the reaction by products are desorbed and exhausted thus minimising the concentration of residues. The separation of the precursor pulses with purge times also prevents reactions and nucleation in gas phase [29]. Once layers A and B have been deposited the process is repeated until the thickness required is achieved. The thickness can be controlled very accurately [30].

2.5. Details of tantala films

IBS and ALD Ta_2O_5 films were supplied by the Commonwealth Scientific and Industrial Research Organisation (CSIRO) allowing for various comparisons to be made with changes in post annealing temperature, TiO_2 dopant levels in films and between deposition methods. The supplied film details are given in Table 2 with the inclusion of a similar PLD film I produced.

Deposition technique	Heat Treatment (°C)	Doping TiO_2 (%)
IBS	None	None
IBS	400	None
IBS	600	None
IBS	600	14.5
IBS	600	55
IBS	100	75
ALD	None	None
PLD	None	None

Table 2 – The key differences of deposition technique, heat treatment and content of TiO_2 in the studied tantala films.

In addition to the films listed in Table 2 I produced thinner PLD films to understand the effect of changing deposition temperature, deposition gas pressure and film thickness on surface roughness measured with AFM. The results are presented in sections 4.1 to 4.6. These films had thicknesses in the range of 10-100nm and were also tested with Raman spectroscopy. However, the films were deemed to be too thin to achieve clear, meaningful Raman spectra. Therefore only one 500nm thick PLD film (last entry in Table 2) was tested with Raman spectroscopy and it serves to make a comparison between similar IBS and ALD tantala films.

A number of comparisons can be made between the films listed in Table 2. The effect of heat treatment and doping with TiO_2 in order to suppress the mechanical dissipation can both be assessed with AFM and Raman spectroscopy. A comparison of different deposition methods can also be made.

3. Film surface roughness assessment

In this chapter I will discuss the theory behind atomic force microscopy (AFM) and how to characterise AFM data.

3.1. Atomic Force Microscopy

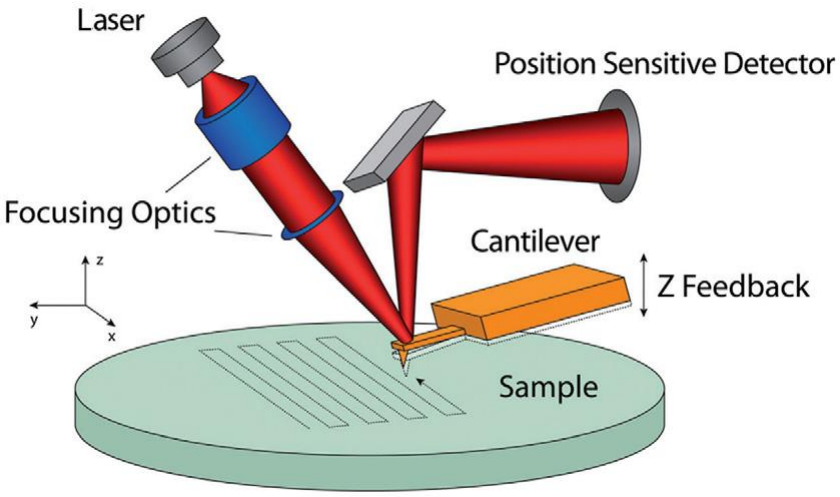

Figure 5 – Overview showing the main components of an AFM. Image taken from reference [31].

Atomic force microscopy (AFM) is part of the family of scanning probe microscopies and is used to measure the topology of film surfaces. A small sharp tip with a width on the order of nm is fixed to the end of an oscillating elastic cantilever. The cantilever is brought into close proximity with a sample surface so as to measure the interactive atomic forces and produce a topographical image. The atomic forces experienced by the tip at the surface can bend the cantilever and reduce the oscillation of its amplitude. The reduced amplitude is used as a feedback and the tip is moved until the amplitude returns to the set point. A beam emitted by a diode laser is aligned on the cantilever and the reflection recorded by a segmented photodetector. Any movement in the cantilever results in the movement of the recorded reflection and a change in the differential signal across the segments [32]. By rastering the tip across the film's surface a picture is built up sequentially of the surface. The lateral resolution of a surface is constrained by the tip curvature and also the sensitivity of the entire system. Atomic scale resolution is therefore possible but sources of noise e.g. acoustic and vibrational noise can reduce this capability [32].

Semi contact, or "tapping mode", operation has been used in my work. In this case the cantilever is excited to near its resonant frequency. When in close proximity to the surface the oscillations are dampened due to a loss of energy from making intermittent contact with the surface. The tip-sample distance is altered to keep the oscillation amplitude constant.

Protrusions from the surface plane reduce the cantilever oscillation while depressions or pits into the film have the opposite effect. This alteration of the amplitude is recorded by computer and correlated to surface features so as to build up a 3D representation of the surface of a material [33].

3.2. AFM data analysis

AFM data of the surface of a film was then analysed by the computer software Gwyddion. This will allow for the corrections of imperfections with the data to present an image as close to the real surface as possible. Gwyddion can also characterise the surface in terms of its roughness which is a key parameter for describing how well the surface will reflect a laser beam. AFM images are typically composed of 512 individual line scans and each line scan is the result of 512 individual measurements.

There are many different ways one can parameterise the surface roughness of a film. However some calculations would lead to a description that could be misleading. It is important to use the correct descriptive parameter over a length scale or area that isn't too big or too small so as to yield a correct representative figure. For instance calculating the root mean square (RMS) value of a surface can be misleading. Two different surfaces could in fact yield the same or similar RMS value [34]. More powerful methods can be implemented to describe surface roughness but as a compromise the roughness average, R_a of the surface was calculated with Gwyddion. The RMS value is possible with Gwyddion but R_a is the more accurate option and so this was employed.

Here is a description of the process of implementing the R_a value calculation with Gwyddion. Let z_j be the height of the j^{th} pixel in a line scan that has average height $\bar{z}$. Therefore r_j is the value of any point on a line scan measured from the mean i.e. a measure of a deviation.

$$r_j = z_j - \bar{z} \qquad \text{Eq.1.}$$

By taking the modulus of the RHS, r_j will always be positive. The roughness average R_a is calculated for each AFM image with the data analysis package Gwyddion. The roughness average, R_a is defined as

$$R_a = \frac{1}{N}\sum_{j=1}^{N}\left|z_j - \bar{z}\right| \qquad \text{Eq.2.}$$

R_a is therefore the average deviation from the mean line and is a measure of the roughness of a film if the line scan is thought to be representative of the entire surface.

4. AFM data of tantala films

In this chapter AFM data of tantala films are presented and analysed. Data are analysed and characterised in terms of surface roughness. AFM data of tantala films deposited by pulsed laser deposition are firstly presented and discussed. This is then followed by AFM data of the supplied ion beam sputtered films.

The data presented (starting with Figure 6) shows an AFM image of a film surface on the left hand side with one line section profile from the middle of the AFM image on the right hand side. The line profile shows the variation in height across the image width.

4.1. Tantala films deposited at 40mTorr O_2 and 25-600°C

Initially four 10nm films of tantala were deposited at 40mTorr O_2 and at 25, 200, 400 and 600°C respectively. This allowed for a dependence of surface roughness on deposition temperature to be elucidated. Figure 6 and Figure 7 show the first and last films in this series and Figure 8 is a plot of the surface roughness values of these films against their respective deposition temperature conditions.

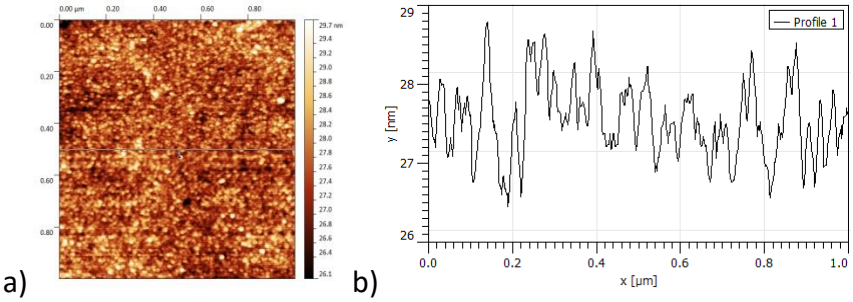

Figure 6 – Tantala film deposited at 25°C and 40mTorr O_2 and a line profile to show the variation of film roughness for one line scan.

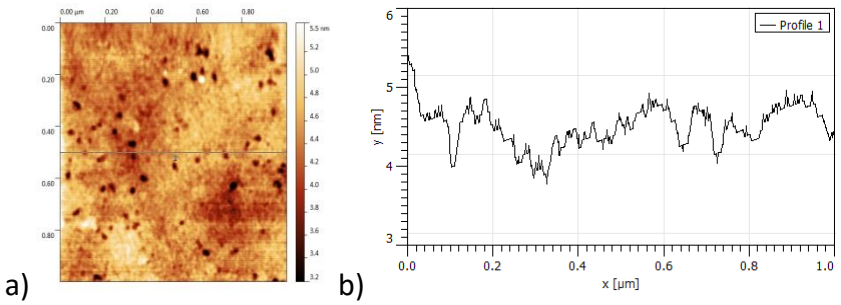

Figure 7 – Tantala film deposited at 600°C and 40mTorr O_2.

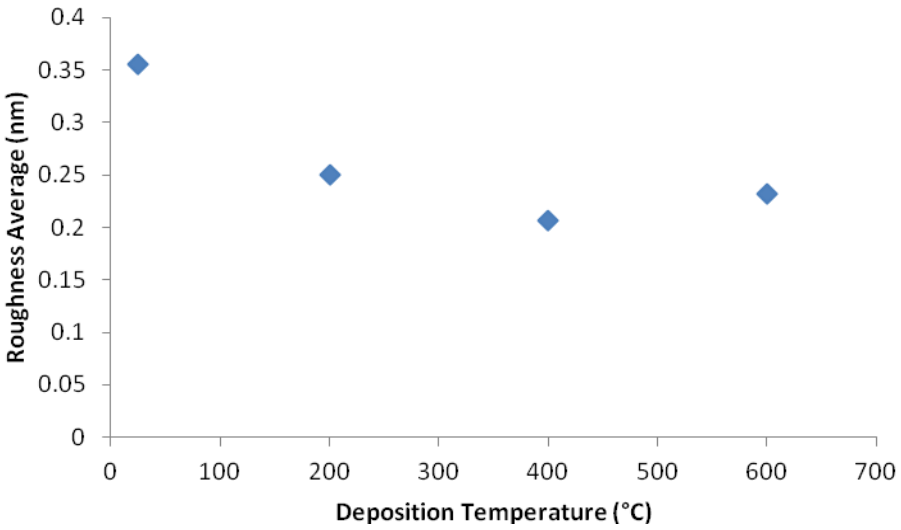

Figure 8 – Roughness average against deposition temperature for 10nm PLD tantala films all deposited at 40mTorr O_2.

The effect of deposition temperature was investigated for PLD tantala films all 10nm thick and deposited in 40mTorr O_2. Figure 6 a) shows an AFM image of a film deposited at room temperature and Figure 6 b) a line profile of the surface. When compared to Figure 7 which corresponds to the last data point in this investigation we notice two things. It would appear that between room temperature and 600°C the surface of the film becomes smoother. This can be seen by comparing the AFM images and seeing that the two line profiles show a larger amplitude variation at 25°C and a much smaller one at 600°C. However pits with an average width of 50nm and a depth of 2nm in the surface become more prevalent towards the 600°C film. In Figure 8 it can be seen that the roughness average value decreases to a minimum at 400°C and then increases slightly towards 600°C.

4.2. Tantala films deposited at 25°C and 0-200mTorr O_2

Five 10nm films of tantala were deposited at 25°C and at 0,1,10,100 and 200mTorr O_2 respectively. This allowed for a dependence of surface roughness on deposition gas pressure to be elucidated. Figure 9 and Figure 10 show the first and last films in the series and Figure 11 is a plot of surface roughness against deposition gas pressure.

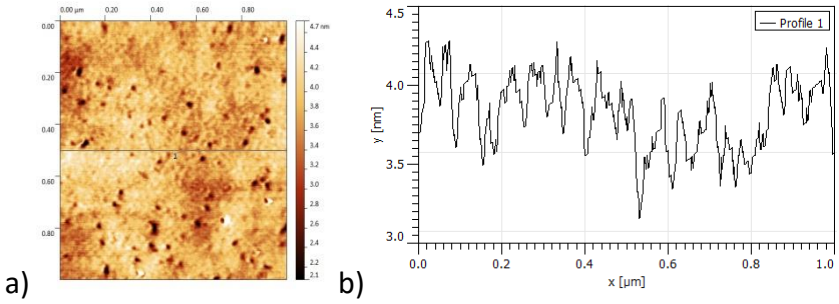

Figure 9 – Tantala film deposited at 25°C and in vacuum.

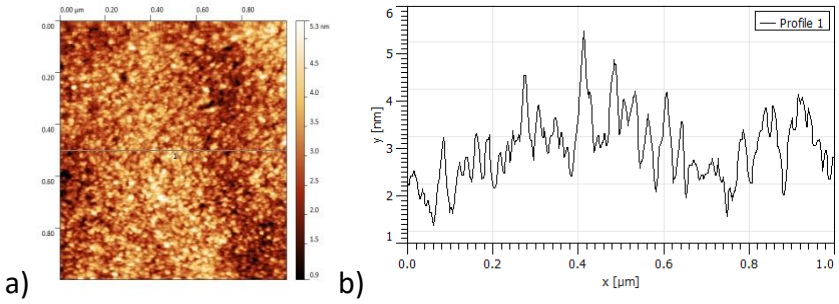

Figure 10 – Tantala film deposited at 25°C and 200mTorr O_2.

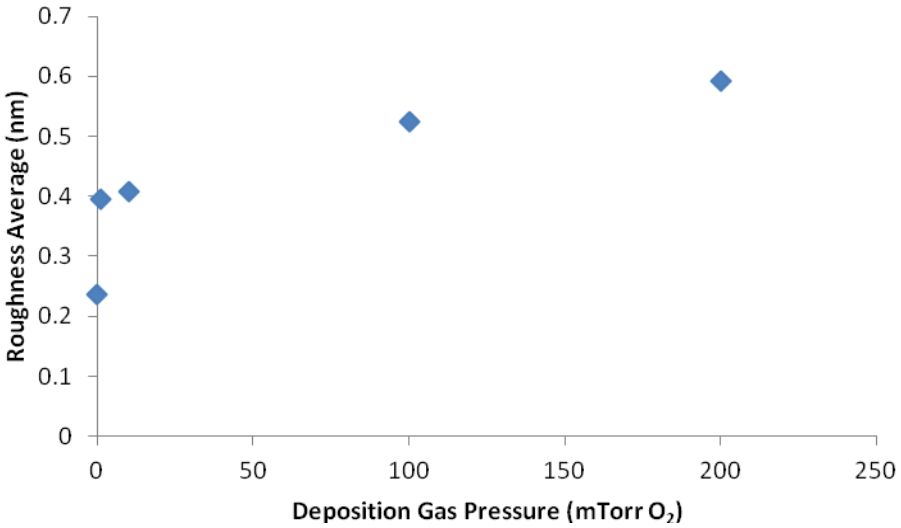

Figure 11 – Roughness average against deposition gas pressure for 10nm PLD tantala films all deposited at room temperature.

The effect of deposition gas pressure was investigated for tantala films all 10nm thick deposited at room temperature. Figure 9 a) shows an AFM image of a film deposited at room temperature in vacuum and Figure 9 b) a line profile of the surface. By comparing to Figure 10 which corresponds to the last data point in this investigation it would appear that between vacuum and 200mTorr O_2 the surface of the films becomes rougher. The prevalence of pits in the surface becomes less with increasing gas pressure. Pits have dimensions of 50-60nm in width and 2nm in depth. By again plotting the roughness average calculated by Gwyddion in Figure 11 it can be seen that the roughness average value increases with increasing gas pressure. With the exception of using vacuum in the first deposition the other data points seem to follow a noticeable trend.

4.3. Tantala films deposited at 25°C and 40mTorr O_2 with increasing film thickness 10-100nm

Six films of tantala were deposited at 25°C and 40mTorr O_2. The film thickness was increased for each film starting with 10nm and increasing to 20, 40, 60, 80 and finally 100nm. This allowed for a dependence of surface roughness on film thickness to be elucidated. Figure 12 and Figure 13 show the first and last films in the series and Figure 14 is a plot of surface roughness against film thickness.

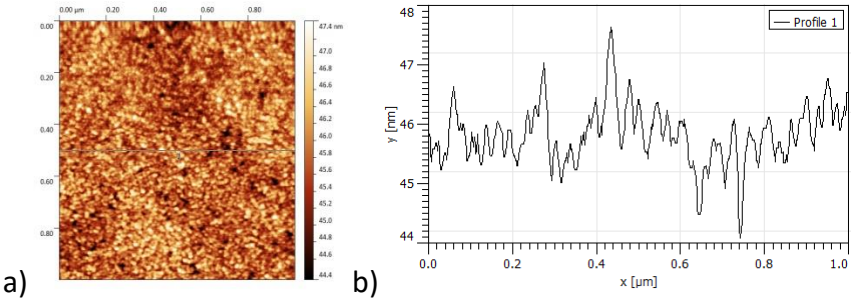

Figure 12 – 10nm tantala film deposited at 25°C and 40mTorr O_2.

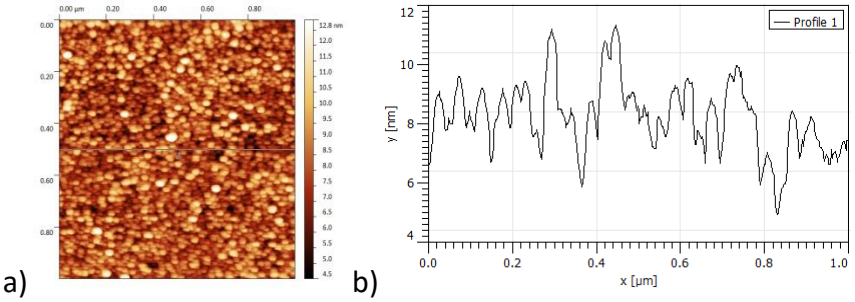

Figure 13 – 100nm tantala film deposited at 25°C and 40mTorr O_2.

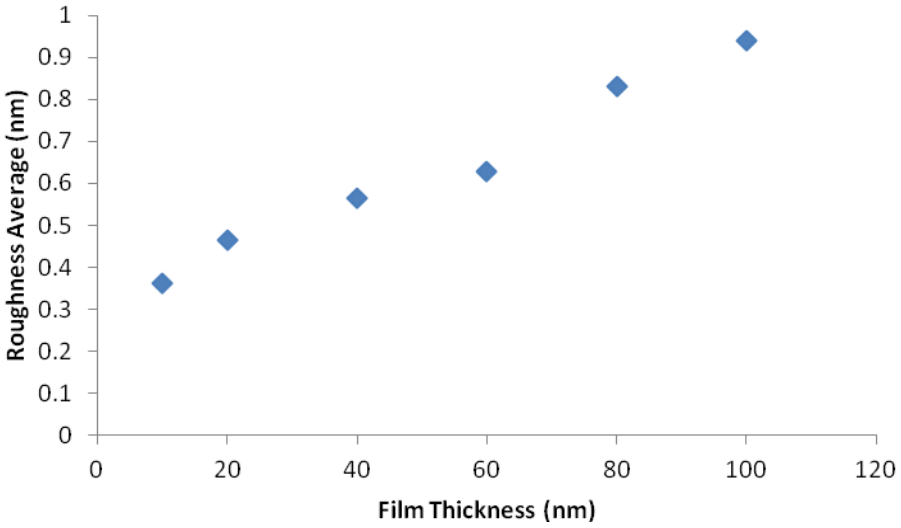

Figure 14 – Roughness average against increasing film thickness for PLD films of tantala.

The effect of increasing film thickness on surface roughness from 10 to 100nm was investigated. Figure 12 a) shows an AFM image of a 10nm film deposited at room temperature and 40mTorr O_2. Figure 13 which corresponds to the last data point in this investigation shows the films become rougher between 10 and 100nm. The occurrence of pits seems to disappear too with increasing film thickness. Pits again were 50nm across and 2nm in depth in Figure 12. By again plotting the roughness average in Figure 14 it can be seen that the roughness average value increases with increasing film thickness. As more and more material is added to a 10nm film on the way to forming a 100nm film the surface becomes exaggerated as material increases both the height and width of each feature observable on the surface. It would also appear that the rate at which the surface roughness increases is not constant. In Figure 14 the roughness average values appear to level off between 40 and 60nm before increasing at almost the same original rate.

4.4. Tantala film deposited at 700°C and 40mTorr O_2

In Figure 15 a drastically different film surface is visible. A 50nm tantala film was deposited at 700°C and 40mTorr O_2.

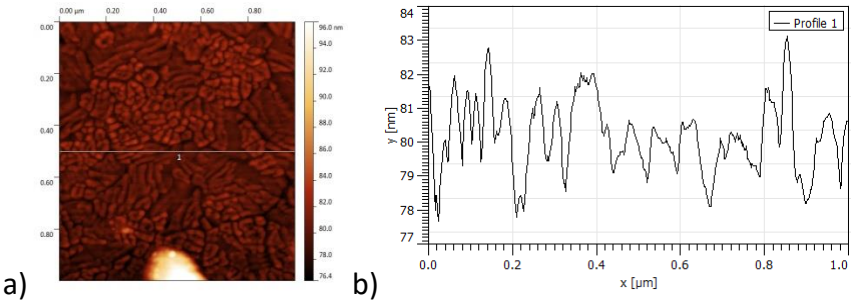

Figure 15 – 50nm tantala film deposited at 700°C and 40mTorr O_2.

Figure 15 shows a surface very different to any other film. Amorphous films of tantala are grown from room temperature to around 800°C where crystallisation takes place. The film in Figure 15 was grown at 700°C and perhaps we are observing with AFM a surface structure change due to this phase transition. It would be interesting and prudent to examine the crystalline structure of this film with TEM to confirm whether or not a new structure has indeed started to form.

4.5. Improved tantala films deposited at 400°C and 1 and 40mTorr O_2

In an effort to see if by combining the conditions presented in 4.1 – 4.3 one could produce even smoother films new depositions were made. Figure 16 shows a 100nm tantala film deposited at 400°C and 1mTorr O_2. For Figure 16 a roughness average value of 0.293 nm was calculated and for Figure 17 a roughness average value of 0.259 nm was calculated.

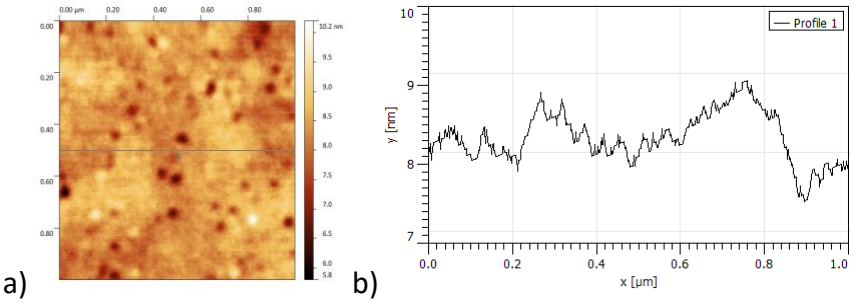

Figure 16 – 100nm tantala film deposited at 400°C and 1mTorr O_2.

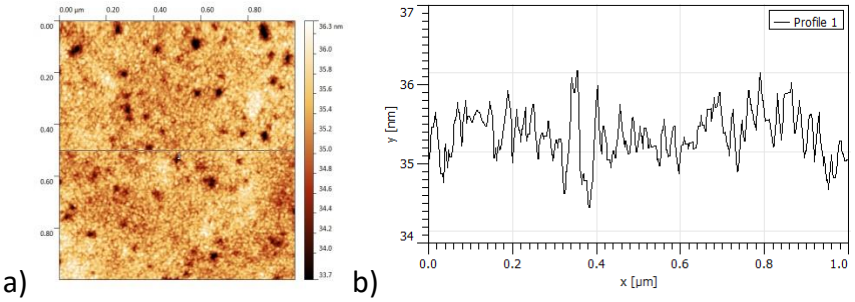

Figure 17 – 100nm tantala film deposited at 400°C and 40mTorr O_2.

In Figures 16 and 17 the appearance and occurence of pits are very similar. In Figure 16 a) pits are ~100nm across and 2nm in depth. In Figure 17 a) they are ~75nm across and 2nm in depth.

4.6. Discussion of AFM data of PLD tantala films

The lowest roughness average for any film belongs to the 10nm tantala film deposited at 400°C and 40mTorr O_2 (section 4.1). Similar roughness values belong to PLD films deposited at 200°C and 40mTorr O_2 and 600°C and 40mTorr O_2 (section 4.1). Also films deposited at 25°C and 0mTorr O_2 (section 4.2) and also the two films deposited at 400°C and 1 and 40mTorr O_2 (section 4.5) have low values. The film in Figure 17 is 100nm thick but 500nm is required for comparisons to IBS and ALD films. The roughness is expected to increase if one deposites a 500nm film from the trend in Figure 14. By combining 400°C and 40mTorr O_2 and depositing a 500nm film it is hoped the smoothest 500nm PLD film would be achieved.

4.7. Heat treated IBS tantala films

Ion beam sputtered tantala films have been deposited and then annealed post deposition. The affect of this treatment is seen here in AFM scans of these film surfaces Figure 19 to Figure 21. Figure 19 shows a film that hasn't been subjected to the heat treatment but it should be noted that the deposition technique deposits the tantala at 100°C.

Figure 22 shows the roughness average values for these three films. It would appear from Figures 19-21 and also from 22 that the roughness appears to decrease with post deposition heat treatment. There is however what looks like some loss of vertical resolution in the line profiles in Figures 19-21 so there will be some error in these values.

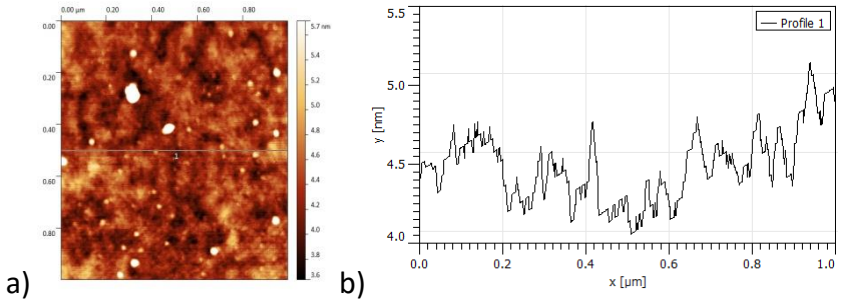

Figure 19 – IBS tantala no heat treatment post deposition.

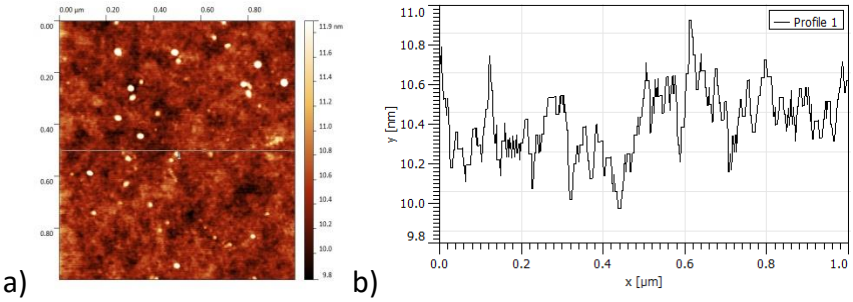

Figure 20 – IBS tantala 400°C heat treatment post deposition.

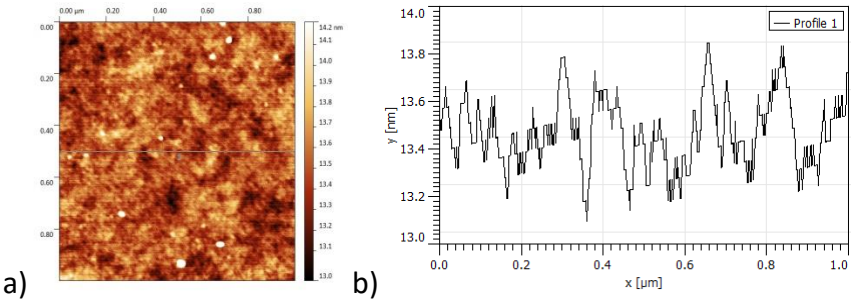

Figure 21 – IBS tantala 600°C heat treatment post deposition.

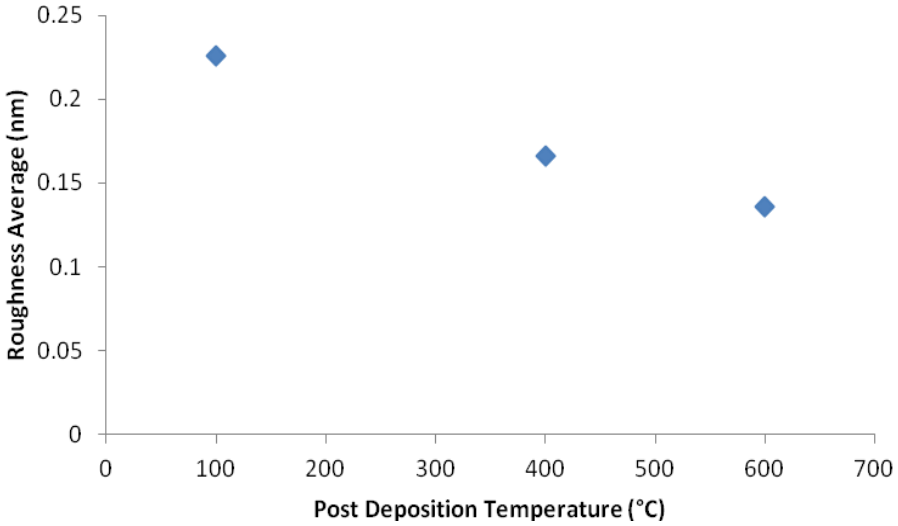

Figure 22 – The roughness average against post deposition heat treatment IBS tantala films.

The average roughness values are 0.226, 0.166 and 0.136nm for Figures 19-21 respectively. It would appear that the surface roughness does decrease with increasing heat treatment temperature. Thermal treatment is key to smoothing out roughness with almost the same trend having been seen with PLD films in section 4.1. Particulates in Figures 19-21 are visible but were excluded from roughness calculations as I deemed them to not be part of the film and were most likely small contaminant particles.

4.8. IBS tantala films doped with TiO_2

Ion beam sputtered films of tantala have also been grown with different levels of the dopant TiO_2 and have also undergone the same post deposition heat treatment. TiO_2 for reduction of mechanical dissipation. Figure 23 shows a tantala film with 14.5% TiO_2 and Figure 24 has a 55% TiO_2 concentration.

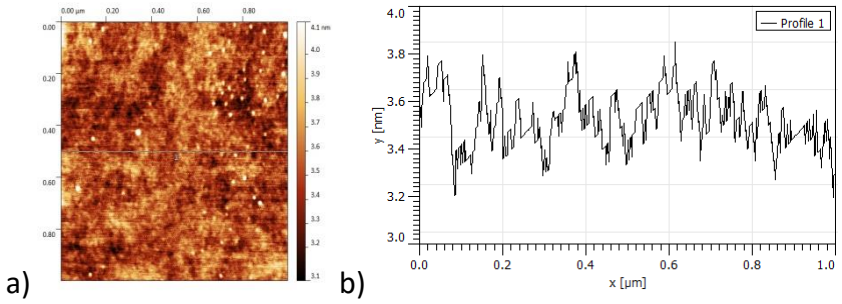

Figure 23– IBS tantala with 14.5% TiO_2 and heat treated post deposition at 600°C

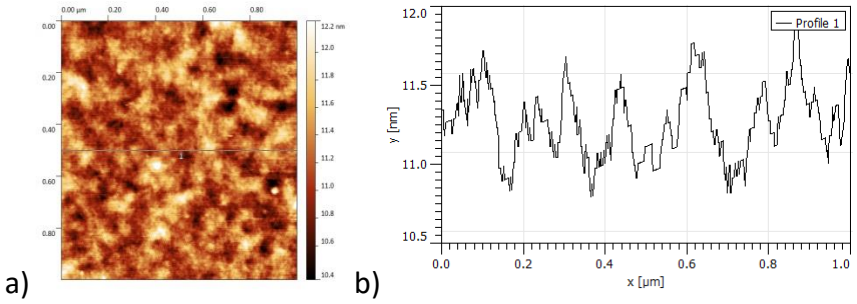

Figure 24 – IBS tantala with 55% TiO_2 and heat treated post deposition at 600°C.

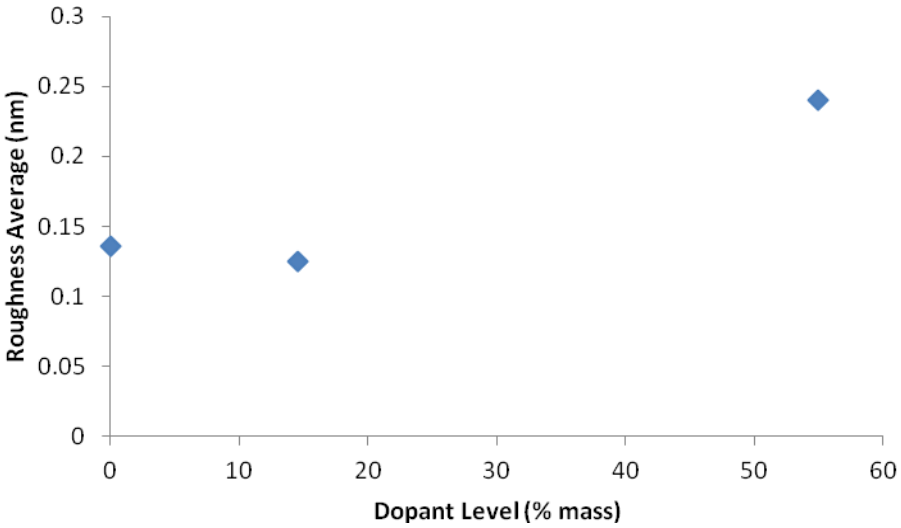

Figure 25 – The roughness average against % dopant level of TiO_2 in tantala films also heat treated post deposition at 600°C.

Differences between the surfaces of Figure 23 and Figure 24 are obvious. By eye the film in Figure 24 appears rougher. The roughness analysis of these films and of a pure IBS tantala film is presented in Figure 25. The roughness values are 0.136, 0.125 and 0.240nm for the 0, 14.5 and 55% dopant levels respectively. So it would appear there is a slight reduction in film roughness for the addition of 14.5% TiO_2 but a much larger increase in surface

roughness for 55% TiO_2. TiO_2 is used to reduce the mechanical dissipation in tantala but seems to also contribute to a rougher surface for IBS films.

4.9. Conclusion of AFM data

AFM was used to study the surface roughness of IBS and PLD tantala films. Some IBS films were heat treated post deposition and some PLD films were deposited in hot environments with the same temperatures used to deposit IBS films. In both cases there is a reduction in roughness up to 400°C. For the IBS films the roughness for the film treated at 600°C is lower than the 400°C case but for the PLD films the 600°C film has a slightly higher roughness value. The IBS films also on the whole have lower roughness values than their PLD counterparts.

5. Raman spectroscopy background theory

Raman Spectroscopy is used to observe the vibrational spectra of materials. This experimental technique can yield "characteristic vibrations" leading to the identification of an unknown material and also give information on its properties [35]. This technique is named after C. V. Raman who in 1928 along with K. S. Krishnan first observed the process [35] - [39]. In Raman Spectroscopy an intense source of monochromatic ultra violet, visible or infrared radiation, typically from a laser, irradiates a sample surface where there is then an exchange of quantised vibrational energy [35]. In the case of my own work a diode laser with a wavelength of 532.17nm was used.

In order to explain the origin of Raman spectra let us consider the classical theory of scattering when photons from a laser interact with the electron cloud of a covalent bond in a molecule [39]. The electric field strength of monochromatic light from a laser can be expressed as a wave varying with time (t)

$$E = E_0 \cos(2\pi\nu_0 t), \qquad \text{Eq. 3.}$$

where the maximum amplitude is E_0 and ν_0 is the frequency.

On illumination with a laser, a dipole is created in the electron cloud of a molecule's bond. The polarisability, P of a bond is related by a proportionality constant, α

$$P = \alpha E = \alpha E_0 \cos(2\pi\nu_0 t). \qquad \text{Eq.4.}$$

When a molecule vibrates at ν_S the normal vibration vector or nuclear displacement with respect to the centre of mass of the molecule is

$$q = q_0 \cos 2\pi\nu_S t, \qquad \text{Eq.5.}$$

where q_0 is the vibrational amplitude.

By expanding the polarisability tensor which describes the polarisability in all directions as a Taylor's series for a small amplitude of vibration, α in terms of q is

$$\alpha = \alpha_0 + \left(\frac{\partial \alpha}{\partial q}\right)_0 q + \cdots \quad , \qquad \text{Eq.6.}$$

where … symbolises the smaller terms I will neglect.

The polarisation can then be fully expressed as

$$P = \alpha_0 E_0 \cos(2\pi \nu_0 t) + \frac{1}{2} E_0 \left(\frac{\partial \alpha}{\partial q}\right) q_0 [\cos(2\pi(\nu_0 - \nu_S)t) + \cos(2\pi(\nu_0 + \nu_S)t)]. \qquad \text{Eq.7.}$$

Equation 7 describes how the induced dipole will oscillate and how three distinct frequencies are emitted when vibrational energy is exchanged in a bond. From Eq.7. the largest term is the first and describes Rayleigh Scattering (also Figure 26 a)) with the second smaller term known as Stokes Scattering (Figure 26 b)) and the last, even smaller, term belonging to Anti Stokes Scattering (Figure 26 c)).

Although the above considers a simple, single covalent bond, it can be expanded qualitatively to the covalent bonding network of an amorphous glass such as tantala. The resultant scattering process is naturally much more complicated. For instance I neglected the tensor aspect and smaller terms in the expansion in Eq.6. denoted by … . A laser beam is the required excitation source as Raman scattering is a weak process being ~10^{-5} of the incident beam intensity and therefore requires the concentrated energy of a laser [37].

To complement the argument on the previous page we must also consider the vibrational energy levels of a bond. From quantum mechanics at ambient temperature the vast majority of atoms exist with a low vibrational energy. According to Boltzmann's law a much smaller number of atoms are in vibrationally excited states [35].

When light in the form of photons interacts with an atom, an electron can be promoted to a virtual state, then decays with the emission of a photon. If the electron decays to its original energy level then the emitted photon has the same energy as the incident one. This interaction has the highest probability of occurring [35]. The photons of the beam each have an energy of $h\nu_0$, where h is Planck's constant and ν_0 the frequency of the energy. The vast majority of photons re-emitted from the material under study are the result of elastic interactions and therefore have the same energy, $h\nu_0$, of the incident beam. This process is known as Rayleigh Scattering (Figure 26 a)) [35] - [39] and this corresponds to the first term in equation 7. However, in a small number of cases the electron is promoted to a virtual energy state and decays to a different energy level to its original one. The emitted photon therefore has a different energy to the incident one. This can either be a photon with energy described as Stokes or Anti Stokes Scattering (Figure 26 b) and c) respectively). This small minority of photon interactions with a sample are inelastic and the re-emitted photons have either a higher energy $h\nu_R = h\nu_0 + h\nu_S$ or lower energy $h\nu_R = h\nu_0 - h\nu_S$ where ν_R is the emitted frequency and ν_S is the frequency change in the inelastic scattering regime.

When the re-emitted photon has energy $h\nu_0$-$h\nu_S$ it is known as Stokes Scattering (2nd term in equation 7) and when the energy is $h\nu_0$+$h\nu_S$ it is known as Anti - Stokes Scattering (3rd term in equation 7). The quantity of $h\nu_R$ is displayed as the Raman Spectrum on a computer screen with the ability to export the data for processing and analysis [35] - [39]. A plot of scattered intensity versus $h\nu_R$ can be used for "finger printing" an obtained spectrum against known standards or models to obtain both the type of substance and the quantity.

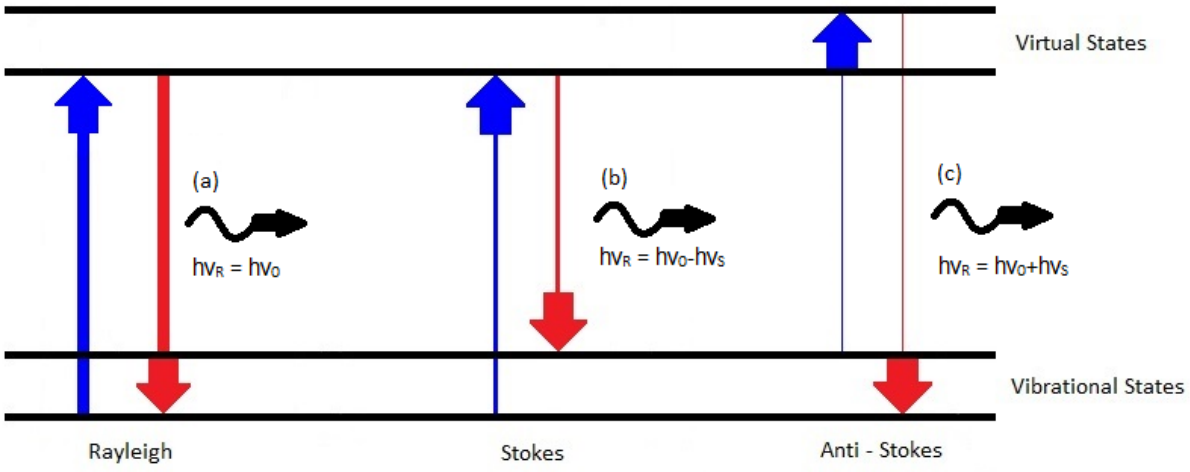

Figure 26 – Vibration energy transitions in a material where the line thickness denotes the relative number of such transitions when a sample is irradiated by a laser.

6. Raman data of tantala films

In this section I will firstly discuss the acquisition of Raman spectroscopy data for tantala films and their associated silicon substrates. I will then proceed to explain how the data can be manipulated to elucidate the features belonging exclusively to tantala alone. Lastly I will discuss these features and present my conclusions.

6.1. Acquisition of Raman data

All the Raman data was collected with a Horiba Scientific Raman spectrometer. In order to collect spectra an optical microscope was used to focus directly on the film surface so as to have the Raman laser interact with the surface of the film.

By increasing and decreasing the height above and below the focus point we were able to see what impact this had on the outputted data. This allowed us to evaluate the error in under or over focusing on the surface. There was very little change in the data with changing the focal point. It can therefore be concluded this had little affect on our data and we can be satisfied that focusing by eye is good enough. We could then proceed to collect data and work on how to process it.

6.2. Analysis method for Raman data

Substantial effort was made in adopting a standard methodology that allowed artefacts to be eliminated from the Raman data and which facilitated the comparison of data acquired from different samples. Figure 27 illustrates the key stages in data manipulation as applied to data acquired from a 500nm thick tantala film on a silicon substrate.

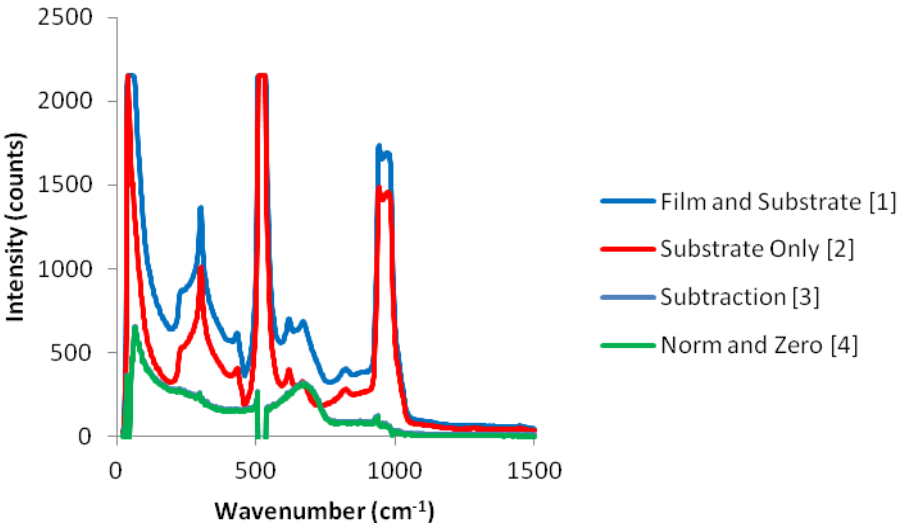

Figure 27 - Four curves showing [1] Raw data which contains Raman spectra belonging to both tantala and silicon. [2] purely silicon data from a substrate. Both [3] and [4] belong to the subtraction, normalisation and zeroing of the data with [3] obscured behind [4].

Raman spectra were acquired for each film and for the silicon substrates. For the tantala films deposited by IBS and ALD the substrate was a silicon cantilever and for the PLD tantala films the substrate was a silicon wafer. The film data includes a contribution from the silicon cantilever or substrate below the film. With the use of a multiplication factor a subtraction can eliminate the silicon components to yield a pure tantala signal.

$$Raman\ (film + substrate) - \chi \cdot Raman\ (substrate) = Raman\ (pure\ tantala) \qquad \text{Eq.8.}$$

The multiplication factor, X in Eq.8. is not frequency dependent. Future effort will be dedicated to a more sophisticated method that has a multiplication factor dependent on frequency in order to completely eliminate any unwanted artefacts.

A choice of filters is available to vary the laser intensity thorough 1, 10, 25, 50 and 100%. The filter strengths are all true apart from the 10% filter which was discovered to actually be 8.6%. The data then has a zero line subtracted from it for a baseline subtraction and the data is normalised by dividing through by the appropriate filter strength.

On the whole the subtraction is successful. However it doesn't always succeed in eliminating all of the silicon features. The peak around 1000cm^{-1} isn't always eliminated for higher powers and the peak around 500 cm^{-1} visible in Figure 27 common to both [1] and [2] simply leaves what appears as a gap in the data when subtraction takes place.

The silicon data obtained is in excellent agreement with existing published literature on the Raman spectrum of crystalline silicon [39] [40]. The tantala data seems to be consistent with recent publications on the Raman spectroscopy study of crystalline and amorphous tantala [41] [42].

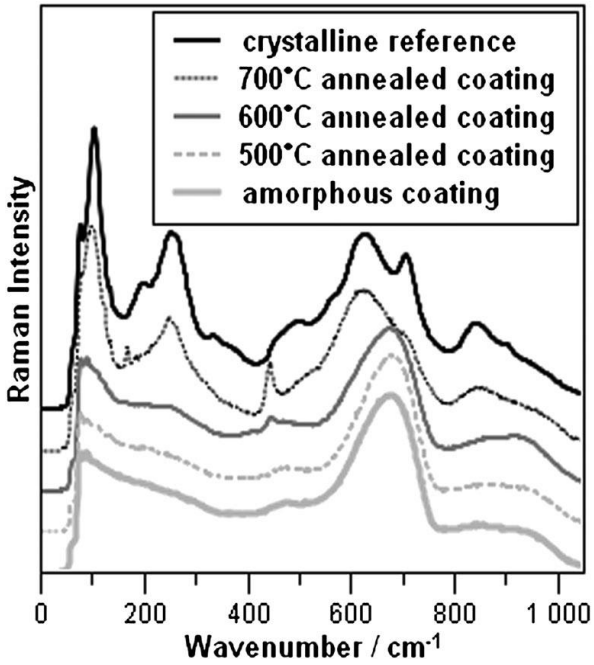

Figure 28 – Raman spectra of tantala films using a 514.5nm Ar laser source. Films have been annealed and the shifting and emergence of peaks is visible with increasing temperature treatment as crystallisation takes place. This figure is taken from reference [42].

Figure 28 is directly taken from [42] and shows the emergence of further structure when a tantala coating undergoes annealing at high temperatures. In Figure 28 we are interested to see the similarity in the Raman spectra of their data and ours (Figure 27). To complement the graph in [42] there is also a detailed description of how different sections of the wavenumber axis correspond to different vibrational modes in the film. The associated intensity then gives the strength of that vibration. Below 150cm^{-1} the vibrational modes are external. Between 150-400cm^{-1} the mode is due to an internal deformation of either the O-2Ta or O-3Ta bond. Between 400-800cm^{-1} the mode is due to internal stretching of the O-3Ta bond. For the region of 800-1000cm^{-1} the mode is due to internal stretching of the O-2Ta bond.

While Raman data was firstly being taken there was concern that there was a change in the spectral readout due to localised heating from the laser which would cause a noticeable

change in the spectra. To check if this was the case readings were taken from the lowest intensity to the highest. The sample was then exposed to the beam at the highest energy for an extended period of time where we were satisfied there was no change in the spectra. The intensity was then lowered again all the while taking readings. It was seen that there was no large change in spectra and therefore no change with any associated heating. A small change was seen and this was attributed to the laser burning off dirt on the film surface.

In the following sections I will present data which show the results from changes in post heat treatment and the inclusion of the dopant TiO_2. I will also show data that show changes between deposition methods. This is hoped to shed light on what conditions and what deposition technique create the best films.

6.3. Thermal treatment of IBS tantala films

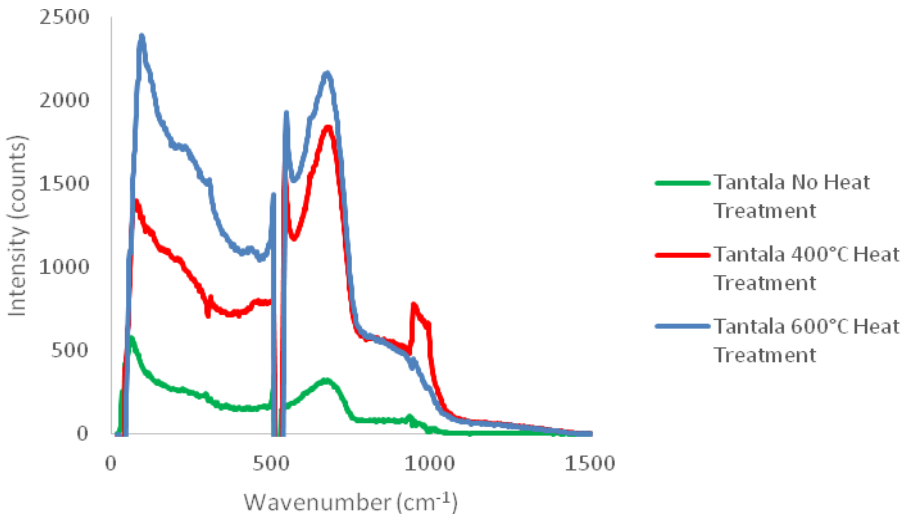

Figure 29 – The effect of a post deposition thermal anneal on films of tantala deposited by IBS.

The lowest intensity curve belongs to the tantala film without any post deposition heat treatment. The intensity of the other two tantala films increases with increasing heat treatment temperature. The first peak intensity for the tantala film treated at 400°C is 2.5 times greater than the no heat film. The first peak for the 600°C treated film is 4.2 times as large. The first peak common to all three curves peaks at approximately 65 cm^{-1} for the no heat treatment film and then shifts slightly to approximately 80cm^{-1} for 400°C and then to approximately 100 cm^{-1} for 600°C.

There is then perhaps an emergence of shoulders or other peaks blended into the large first peak which are most prominent at the higher temperature treatment data. At around 500cm^{-1} there is the start of a very large peak which then becomes negative. This is main

Rayleigh scattering peak common to all data. This apparent absence of data is due to the subtraction process not working well at this point.

The second peak exists at more or less the same wavenumber value of 675 cm^{-1} for each thermal treatment curve. The 400°C is 5.8 times higher than the no heat curve and the 600°C is 6 times higher. If we compare the first peak with the second peak we see that for the no heat treatment case and the 600°C heat treatment case it is lower than the first peak. However for the 400°C case it is much larger. For the no heat case the first peak is 1.77 times greater than the second. For the 400°C case the second peak is 1.31 times larger than the first. For the 600°C case the first peak is 1.1 times larger than the second.

6.4. IBS tantala films doped with TiO_2 and post annealed at 600°C

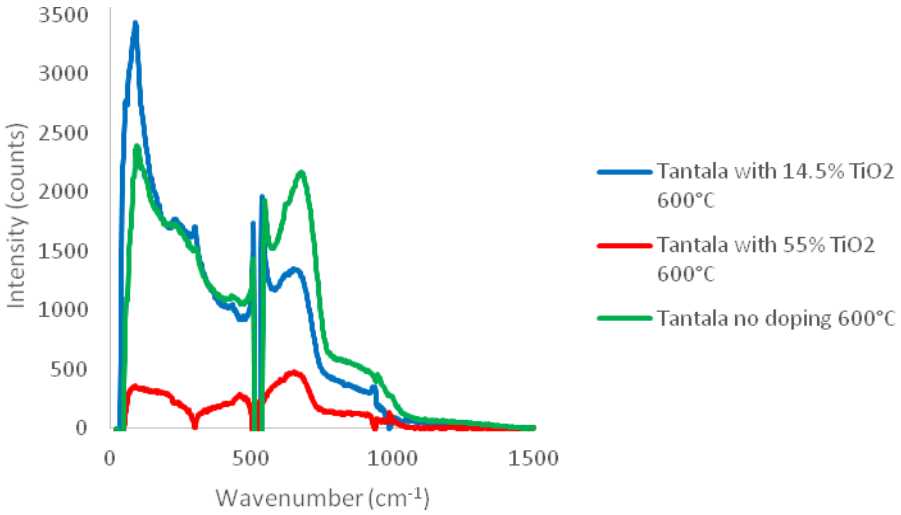

Figure 30 - Comparing no TiO_2 with high and low levels of TiO_2 in tantala films all of which have been treated at 600°C post deposition.

There is a first peak common to all 3 films. The TiO_2 14.5% doped film first peak occurs at ~90cm^{-1}. For the as deposited film it exists at ~100cm^{-1} and then for the TiO_2 55% doped it exists at ~80cm^{-1}. The lowest intensity peak belongs to the TiO_2 55% doped film with the no heat treatment being 6.55 times bigger and the 14.5% being 9.50 times bigger. A second peak exists and for the no heat film at ~675cm^{-1}, ~655cm^{-1} for the 14.5% case and ~650cm^{-1} for the 55% case. The 55% curve has the lowest intensity with the no heat being 4.50 times larger and the 14.5% case being 2.86 times larger. For the no heat case the first peak is 1.16

times bigger than the second. For the 14.5% case the first peak is 1.74 times bigger and for the 55% case the second peak is 1.32 times bigger.

6.5. IBS tantala films doped with TiO_2 and post annealed at 100°C

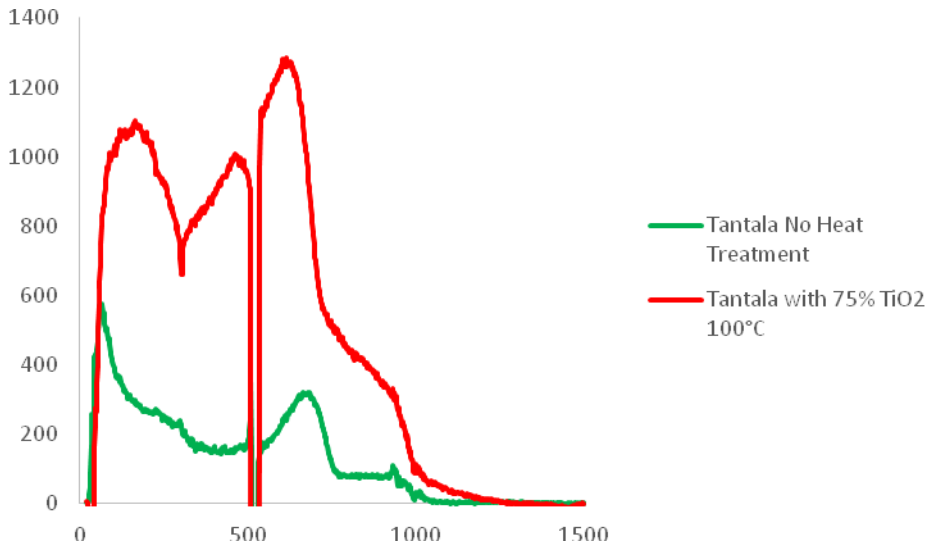

Figure 31 - Comparing no TiO_2 with a high level of TiO_2 doping in tantala films all of which have been treated at 100°C post deposition.

The first peak for the 75% case is much broader than all the other initial peaks so far presented. It exists at 165cm^{-1} and is also 1.98 times bigger than the no TiO_2. The no TiO_2 exists at 65cm^{-1}.

There is what could possibly be another peak or simply an artefact from the subtraction method at ~460cm^{-1}.

The second peak for the 75% case is bigger than the no dopant film by 4.07 times. A slight shift occurs between the two films for this peak with the 75% case having a peak at 620cm^{-1} and the control at 665cm^{-1}.

6.6. IBS tantala films compared to an ALD tantala film

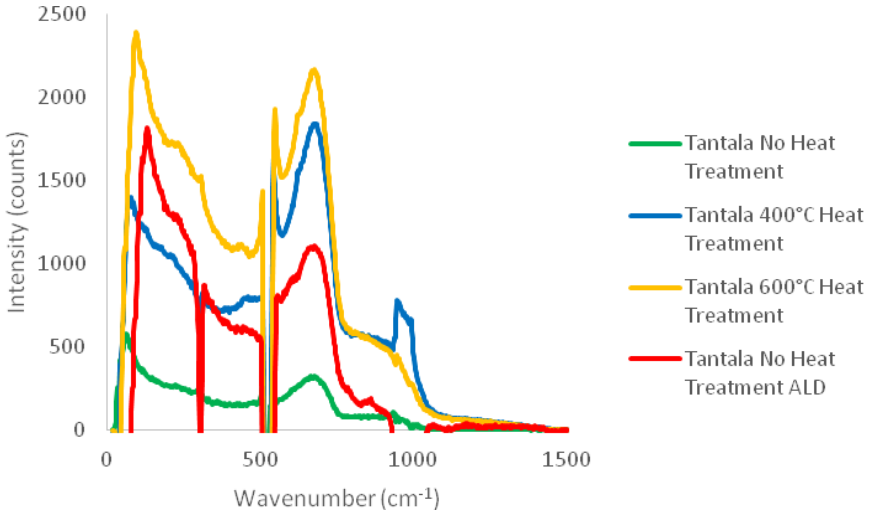

Figure 32 - Ion Beam Sputtered films compared with Atomic Layer Deposition film.

The same trend as was seen in Figure 28 is repeated here. However there is the inclusion of a tantala film deposited by atomic layer deposition. The first peak of the ALD film occurs at ~125 cm^{-1} and it exists between the 600°C and 400°C curves being 3.4 times as high as the no heat data.

Again the same trend is repeated for the second peak as in Figure 28. The ALD second peak occurs at ~677 cm^{-1} which is identical to the other films being 3.5 times as high as the no heat treatment film.

When comparing the two peaks the same trend is seen and for the ALD sample the first peak is 1.71 times bigger than second.

6.7. PLD tantala film

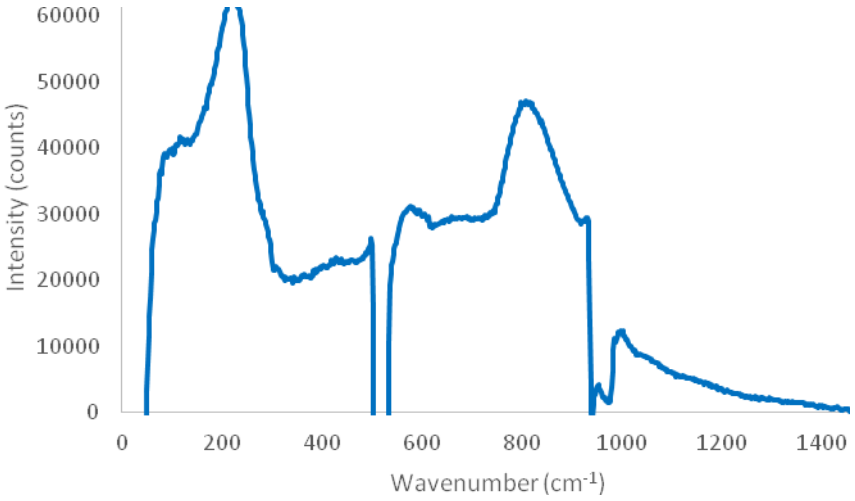

Figure 33 - Pulsed Laser Deposition film of tantala.

The first peak occurs at ~220cm^{-1} which is at a higher energy than for the other films. The second peak exists at ~800cm^{-1} which is again at a higher energy than in the other films. The film presented in Figure 32 had the same thickness as the other films ~500nm. Much thinner PLD films were produced but when it came to Raman analysis they were too thin to produce a meaningful spectrum with identifiable features.

6.8. Comparing IBS, ALD and PLD

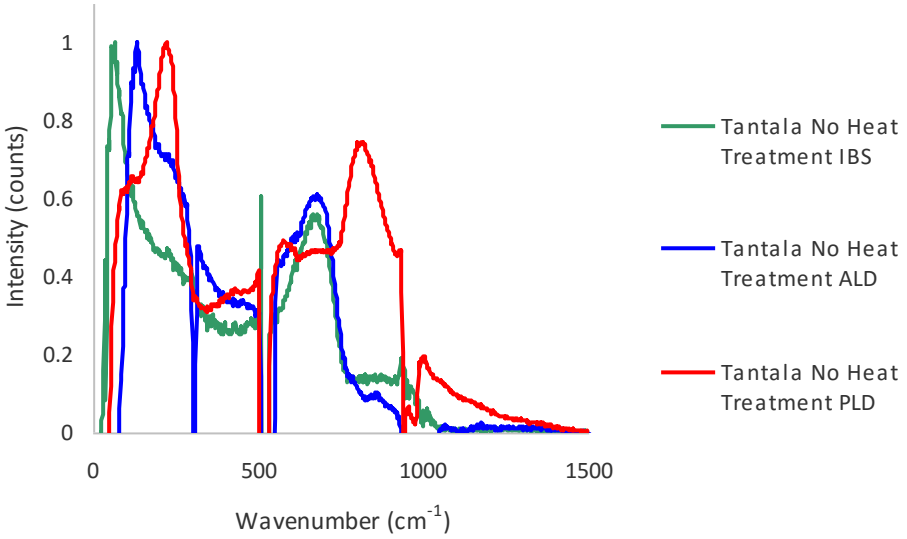

Figure 34 – Comparison in Raman data between similar films only differing in deposition technique.

The data in Figure 34 had to be normalised as the PLD spectrum intensity was originally much too great compared to the rest. In Figure 34 I directly compare the Raman spectra of 3 films each deposited by a different deposition technique. The first peak is similar in each case but there is a shift towards higher energies from IBS at 65cm^{-1} to ALD at 132 cm^{-1} to PLD at 222cm^{-1}.

The second peak is very similar for both the IBS and ALD cases. Both peaks seem to occur at 685cm^{-1} with the ALD peak being slightly higher than the IBS film. The PLD peak occurs at a much higher energy of 816$cm^{-1}$with a greater intensity.

6.9. Discussion of Raman data

Tantala films have been analysed with Raman spectroscopy. Changes in deposition technique, post deposition thermal annealing and levels of doping of TiO_2 have all been assessed.

The first peak appears to be broadly consistent throughout the variations amongst the films. However there are key differences to note. In Figure 30 the spectra for the film with a TiO_2 dopant level of 14.5% begins to show a curvature close to the tip of the first peak. As the TiO_2 dopant level is increased to 55% we see a structure with less pronounced peaks and at a much less intensity. This structure is identical to the 75% TiO_2 doped film in Figure 31. Perhaps we can conclude that with increasing levels of TiO_2 in tantala films you get a broadening and reduction in intensity of this first peak.

It would also appear that the first peak for the ALD sample in Figure 32 is identical yet shifted to a higher energy. In Figure 33 there is Raman data for a tantala film deposited by pulsed laser deposition. There is similar structure but the first peak isn't the same as in the other plots. This could be due to the deposition method being different or because it might be a different oxide of tantala. This film was produced at 1mTorr O_2 much lower than the 40mTorr O_2 figure quoted in the literature for Ta_2O_5 [7]. An assessment of its oxide content has not yet been established but perhaps this may have a different chemical structure.

In Figure 30 the addition of the TiO_2 to 14.5% seems to reduce the second peak and increase the first. Increasing the dopant level to as much as 55% TiO_2 dramatically changes the spectrum and yields a two peak structure with much lower intensity.

The first peak corresponds to deformation and stretching of O-2Ta and O-3Ta and the second peak corresponds to purely stretching of O-2Ta and O-3Ta. In Figure 28 heat treatment appears to increase the overall intensity and also produce a stronger stretching mode of O-2Ta and O-3Ta. This seems to be in agreement with the data presented in Figure 28 from reference [42].

In Figure 30 the inclusion of TiO_2 to 14.5% appears to suppress the stretching of O-2Ta and O-3Ta above 500cm^{-1}. It does however appear to promote the deformation and stretching of O-2Ta and O-3Ta at modes below 500cm^{-1}. With the addition of TiO_2 to 55% both types of vibration are suppressed to the lowest level for that series. This could perhaps back up the assertion from reference [15] about TiO_2 reducing noise in Ta_2O_5 films. However there is what appears to be contradictory behaviour displayed in Figure 31 as the film with TiO_2 included to 75% has an overall higher intensity than the pure Ta_2O_5 film. This may suggest the need to include the post deposition thermal treatment.

Considering Figures 32-34 and the comparisons between the similar IBS, ALD and PLD films it would appear that IBS has the lowest overall intensity. The second highest intensity then belongs to ALD and then the highest to PLD. There is a similarity between IBS and ALD films but the PLD film appears to have peaks shifted to higher energies.

7. Conclusion

Tantala films have been studied with AFM and Raman spectroscopy. These tantala films have to have a low film surface roughness and Raman spectra with low intensity vibrational modes. Both of these criteria should assist in making tantala films good candidates for mirror coatings in gravitational wave detectors.

PLD and IBS films were both analysed with AFM. Changes in heat treatment, gas pressure and film thickness were investigated for PLD tantala films to try and minimise surface roughness. Films with that combined a low gas pressure and elevated deposition temperature seem to exhibit the best features. The film deposited at 400^{o}C and 40mTorr O_2 had the lowest roughness.

IBS tantala films underwent thermal treatment and doping with TiO_2. The IBS films all had a lower surface roughness than the PLD films with the tantala film post annealed at 600^{o}C with 14.5% TiO_2 having the lowest overall roughness. We can say that an elevated temperature is crucial for smoothing out any roughness for both deposition techniques.

The majority of the Raman data was taken from studying the IBS films. One ALD and one PLD film were also included to facilitate the comparison of other deposition techniques. Heat treating the films appeared to yield a more intense Raman spectrum. Doping up to 14.5% TiO_2 appeared to increase the first peak and reduce the second peak. By increasing the TiO_2 content to 55% TiO_2 both peaks appear to have been dramatically reduced. This was not the case for the lower temperature anneal and 75% doping film. It may well then be the case that a combination of elevated temperature and doping with TiO_2 can indeed lower the intensity of certain vibrational modes.

IBS films have a lower Raman spectroscopy intensity than ALD and PLD with the ALD film having a similar spectrum to the IBS film annealed at 400^{o}C. The PLD film differs the most from IBS and ALD with both characteristic tantala peaks being shifted to higher energies.

By considering both types of data presented in this report it would appear that IBS films appear to be the best overall candidates for mirror coatings. They give the lower surface roughness and the lower Raman spectroscopy intensity spectra.

Research will continue in this area and there will also be a publication with some of these results included.

8. References

[1] S. Boughaba, G.I. Sproule, J.P. McCaffrey, M. Islama, M.J. Graham. 2000. Thin Solid Films, 358, 104-113.

[2] Y. Nishimura, K. Tokunaga, M. Tsuji. 1993. Thin Solid Films, 226, 144-148.

[3] Y. Nishimura, U. Hiroki, T. Ochiai, M. Tsuji. 1994. Applied Surface Science, 79/80, 165-170.

[4] S. K. Zhang, Z. W. Fu, L. Ke and F. Lu, Q. Z. Qin, X. Wang. 1998. Journal of Applied Physics, 83 (11), 6082-6088.

[5] Q. Qin, Z. Fu. 1999. Advanced Materials, 11 (13), 1119-1123.

[6] S. Boughaba, M. U. Islam, G. I. Sproule, M. J. Graham. 1999. Surface and Coatings Technology, 120-121, 757-764.

[7] Zs. Geretovszky, T. Szorenyi, J.-P. Stoquert, I.W. Boyd. 2004. Thin Solid Films, 453 –454, 245–250.

[8] X. He, J. Wu, X. Li, X. Gao, L. Wu, L. Zhao, X. Gan, F. Zhuge. 2009. Thin Solid Films, 518, 94–98.

[9] X. Hea, J. Wu, X. Li, X. Gao, X. Gana, L. Zhao. 2009. Journal of Alloys and Compounds, 478, 453–457.

[10] R. R. Krishnan, K.G. Gopchandran, V.P. MahadevanPillai, V. Ganesan, V. Sathe. 2009. Applied Surface Science, 255, 7126–7135.

[11] J. Zhang, Q. Fang, I. Boyd. 1999. Applied Surface Science, 138-139, 320-324.

[12] Z. Mingfei, F. Zhengwen, Y. Haijun, Z. Zhuangjian, Q. Qizong. 1997. Applied Surface Science 108, 399-403.

[13] J. Hough, S. Rowan. 2005. J. Opt. A: Pure Appl. Opt. 7 (2005) S257–S264.

[14] I. W. Martin et al. 2010. Class. Quantum Grav. 27 (2010) 225020.

[15] G. M. Harry et al. 2007. *Class. Quantum Grav.* 24, 2, 405-415.

[16] R. P. Netterfield et al. 2005. *Proc. SPIE* 5870 58700H.

[17] K. Numata, K. Yamamoto, H. Ishimoto, S. Otsuka, K. Kawabe, M. Ando, K. Tsubono. 2004. *Phys. Lett.* A, 327, 263–71.

[18] Smith, H. M., 1965. Appl. Opt. 4 (1), 147-148.

[19] Dijkkamp, D., 1987. Appl. Phys. Lett. 51 (8), 619-621.

[20] L.W. Martin, Y.-H. Chu, R. Ramesh. 2010. Materials Science and Engineering R 68, 89-133.

[21] T. Hinoa, M. Nishida, T. Araki. 2002. Surface and Coatings Technology 149 (2002) 1–6.

[22] Z-W. Fu, F. Huang, Y-Q. Chu, Y. Zhang, Q-Z Qin. 2003. *Journal of The Electrochemical Society*, 150 (6) A776-A782.

[23] Y. Nishimura, H. Ujita, M. Tsuji. 1995. Applied Surface Science 89 393-399.

[24] A. F. Stewart, S. M. Lu, M. M. Tehrani, C. Volk. 1994. The international society for optics and photonics, 2114, 662-667.

[25] T. Kaneko, N. Akao, N. Hara, K. Sugimoto. 2005. Journal of The Electrochemical Society, 152 (4), B133-B139.

[26] C. L. Tien. 2008. Applied Surface Science, 255, 2890-2895.

[27] J-W. Lim, Y. Ishikawa, K. Miyake, M. Yamashita, M. Isshiki. 2002. Materials Transactions, 43 (3), 478-481.

[28] J. R. McNeil, A. C. Barron, S. R. Wilson, W. C. Herrmann. 1984. APPLIED OPTICS, 23 (4), 552-559.

[29] K. Kukli, M. Ritala, R. Matero, M. Leskelä. 2000. Journal of Crystal Growth, 212, 459-468.

[30] S. M. George. 2010. Chem. Rev, 110, 111-131.

[31] N. A. Geisse. 2009. Materials today, volume 12, number 7-8.

[32] Mironov, V. L., 2004. Fundamentals of Scanning Probe Microscopy. THE RUSSIAN ACADEMY OF SCIENCES INSTITUTE OF PHYSICS OF MICROSTRUCTURES Nizhniy Novgorod: NT-MDT.

[33] C.B. Prater, P. G. Maivald, K.J. Kjoller, M.G. Heaton. 2004. Tapping Mode Imaging Applications and Technology. Veeco Instruments Incorporated.

[34] Duncan, D., 2008. AFM measurements of the roughening of Cysteine on Gold. Thesis (MSci.). The University of Glasgow, Glasgow.

[35] D. Bougeard, M. Buback, A. Cao, K. Gerwert, H. M. Heise, G. G. Hoffmann, B. Jordanov, W Kiefer, E.-H. Korte, H. Kuzmany, A. Leipertz, E. Lentz, J. Liquier, A. Roseler, H. Schnockel, B. Schrader, H. W Schrotter, M. Spiekermann, E. Taillandier, H. Willne. Edited by B. Schrader. 1995. Infrared and Raman Spectroscopy. VCH Verlagsgesellschaft mbH, Weinheini (Federal Republic of Gcrmany) and VCH Publishers. Inc., New York, NY (USA).

[36] D. A. Long. The Raman Effect A Unified Treatment of the Theory of Raman Scattering by Molecules. 2002. John Wiley & Sons Ltd, Baffins Lane, Chichester, West Sussex PO19 1UD, United Kingdom.

[37] J. R. Ferraro, K. Nakamoto, C. W. Brown. 2003. Second edition. Introductory Raman Spectroscopy. Elsevier Science (USA).

[38] E. Smith, G. Dent. 2005. Modern Raman Spectroscopy A Practical Approach. John Wiley & Sons Ltd, The Atrium, Southern Gate, Chichester, West Sussex PO19 8SQ, United Kingdom.

[39] M. S. Amer. 2010. Raman Spectroscopy, Fullerenes and Nanotechnology. The Royal Society of Chemistry, Thomas Graham House, Science Park, Milton Road, Cambridge CB4 0WF, United Kingdom.

[40] P. A. Temple, C. E. Hathaway. 1973. VOLUME 7, NUMBER 8, 3685-3697.

[41] J.F. Meng, K. R. Brajesh, R.S. Katiyar, A. S. Bhalla. 1997. Volume 58, Number 10, 1503-1506.

[42] H. Ono, Y. Hosokawa, K. Shinoda, K. Koyanagi, H. Yamaguchi. 2001. Thin Solid Films 381. 57-61.

[43] C. Joseph, P. Bourson, M. D. Fontana. 2011. Journal of Raman Spectroscopy, 43, 1146-1150.